Grain size characterization in metallic alloys using different microscopy and post-processing techniques

Baptiste Flipon, Victor Grand, Brayan Murgas, Alexis Gaillac, Alexis Nicolaÿ, Nathalie Bozzolo, Marc Bernacki

Version of Record: https://www.sciencedirect.com/science/article/pii/S1044580321001078
Manuscript_e106f47c1784ec46d01f027e795b9b64

Grain size characterization in metallic alloys using different microscopy and post-processing techniques

B. Flipon[a,*], V. Grand[a,b], B. Murgas[a], A. Gaillac[b], A. Nicolaÿ[a], N. Bozzolo[a], M. Bernacki[a]

[a] *Mines ParisTech, PSL - Research University, CNRS, CEMEF, UMR 7635, 06904 Sophia Antipolis, France*
[b] *Framatome - Research center Zr components, 73400 Ugine, France*

Abstract

In this work, an image analysis procedure which enables an estimation of grain size distribution from optical and scanning electron micrographs is detailed. Two applicative cases (a face centered cubic austenitic stainless steel and a hexagonal close packed zirconium alloy, both with fully recrystallized equiaxed microstructure) are considered. Grain size definition is discussed both in terms of mean grain size and of grain size distribution. Classical methodologies as well as standardized definitions are recalled and compared to each other. Results obtained by electron backscattered diffraction analysis are compared to the ones obtained after image analysis based on backscattered electron or optical micrographs. The effect of data processing parameters on grain size results is also examined. Image analysis based on optical or scanning electron micrographs proves to be suitable to obtain accurate grain size distribution information with shorter acquisition and processing times compared to EBSD orientation mapping of the same analyzed area.

Keywords:
Mean grain size, Grain size distribution, Optical Microscopy, Scanning Electron Microscopy, BackScattered Electron, Electron BackScattered Diffraction, Image analysis

1. Introduction

The Grain Size (GS), or more generally the Grain Size Distribution (GSD), is one of the main microstructural characteristics of a metallic alloy, in particular because it is determinant for mechanical properties [1, 2, 3]. From an industrial point of view, controlling microstructural evolutions during forming processes has become an essential aspect in the development of alloys with targeted specific in-use properties. What is *grain size* and how to define it rigorously, both considering raw data acquisition and post-processing techniques are relevant questions to ensure coherent and comparable quantities between studies on the

*Corresponding author
Email address: baptiste.flipon@mines-paristech.fr (B. Flipon)

same material and also between different published works.

A metallic alloy is a 3D polycrystalline aggregate. This 3D microstructure can be complex and information related to the (3D) grain size might be missing after the sectionning of the observation surface. In samples with equiaxed grain microstructures, the use of a stereologic method (such as the Saltykov's one [4, 5]) can be sufficient to correctly estimate the 3D GSD, especially regarding the mean and the upper part of the GSD [6]. Since 2D sectionnal observations still remain the standard for grain size analyses, a particular focus will be made on microscopy and post-processing techniques used for grain size characterization considering 2D observation surfaces.

In relatively homogeneous and equiaxed microstructures, the Mean Grain Size (MGS) is often used as the main microstructure descriptor. Several quantities can be used behind the *grain size* terminology, such as the mean intercept length [7, 8], the equivalent circle diameter [9] or the ASTM grain size [10] for example. When the acquisition or post-processing techniques enable it, working directly with GSD provides more information, in particular regarding the spread around MGS or the description of multimodal microstructures. With GSD and their associated parameters, microstructure description is more accurate, which can be especially relevant for studying microstructure evolution induced by recrystallization and related phenomena or for polycrystal generation in the context of full-field microstructure modeling [11, 12]. Regarding microstructural simulations, precise GSD information are one of the mandatory experimental data used to generate initial microstructures and perform material parameters identification associated with microstructure evolutions. The latter usually requires numerous microstructural observations and will benefit from both reduced acquisition time and improved accuracy compared to other microscopic methodologies.

With recent development and improvement of scanning electron microscopy techniques, grain size measurements have gained in accuracy. The Electron BackScattered Diffraction (EBSD) technique in a Scanning Electron Microscope (SEM) can provide precise GSD information based on crystallographic orientations even considering ultrafine-grained microstructures [13] or deformed materials [14]. EBSD also enables the quantification and characterization of grain boundaries (special grain boundaries such as $\Sigma 3$ twin boundaries for example) and to access local misorientation quantities using parameters such as the Kernel Average Misorientation (KAM) that give an insight onto Geometrically Necessary Dislocations (GND) densities. For coarse grained materials, Optical Microscopy (OM) or BackScattered Electron (BSE) imaging in the SEM enable larger view fields and shorter acquisition times compared to EBSD and may thus lead to a better accuracy regarding statistical representativity.

Grain size measurements by EBSD have been covered by Humphreys [15] with a particular emphasis on grain and subgrain sizes in [16]. Wright [17] also proposed a detailed and complete sensitivity study of both acquisition and analysis parameters considering grain size measurements with EBSD. Day and Quested [18] presented microscopy imaging based on

orientation contrast (Orientation Contrast Imaging (OCI)) and compared these techniques with both optical metallographic observations and EBSD. Conclusions are then drawn from direct comparisons between the imaging techniques considering the mean linear intercept: results are similar in terms of mean intercept length but differs in terms of accuracy regarding grain boundary detection, crystallographic informations and processing time. OM can provide a decent estimation of the MGS for a limited analysis time. Another crystal orientation mapping technique based on the analysis of the channeling contrast under both ion [19] and electron [20] beams has been developed by Langlois and coworkers. The tilted sample is rotated in the SEM chamber, and secondary electron (SE) / backscattered electron (BSE) images are acquired after a fixed rotation step (360 images for a 360° rotation with a 1° step for instance). Intensity profiles (as a function of rotation angle) are then compared to theoretical profiles in order to deduce the crystallographic orientation at each point of the analyzed area. This alternative technique to EBSD also enables to perform automatized image analysis with edge detection in order to extract Grain Boundaries (GBs) and thus GSDs. A similar method, relying on crystallographic orientation contrasts, is proposed in this paper to obtain GSD information from optical and BSE micrographs. The final purpose being to have a general user-friendly procedure based on grey-scale imaging that enables a precise estimation of GSD with a limited acquisition time. Results are compared with those of the mean intercept length [7, 8] for MGS evaluation and with those of EBSD analyses regarding GSD.

The paper is organized as follows. Section 2 is dedicated to the introduction of the materials, equipments and analysis / post-processing techniques used to determine grain sizes in this work. Section 2 also includes two subsections dedicated to MGS evaluation and GSD representation. Section 3 presents and compares results from different microscopy techniques, MGS / GSD being obtained using several processing treatments. These results are then discussed in terms of time (preparation, acquisition, post-processing) and of accuracy in Section 4. Conclusions are finally pointed out in Section 5.

2. Materials and methods

2.1. Materials and samples preparation

Two metallic alloys have been used in this work: Hexagonal Closed-Packed (HCP) Zircaloy-4 (Zy-4) and Face Centered Cubic (FCC) 304L austenitic stainless steel.

The Zy-4 alloy is a nuclear-grade one with a conventional chemical composition: >95 wt% in Zr, ∼2 wt% of Sn, Cr, Fe (Ni and Nb can also be found) and low amounts of residual Hf (<0.01 wt%). Sample preparation consists first in automatic mechanical grinding down to SiC papers with a grit size of 30 µm (P600), polishing with a diamond suspension solution (15 µm) and then fine polishing with a solution composed of 7 mL of OPS colloidal silica, 3 mL of H_2O_2 and small amount of HF (between 5 and 10 droplet) in order to reveal grains under polarized light.

The 304L austenitic stainless steel chemical composition is 8.0 wt% Ni, 18.0 wt% Cr, 0.09 wt% N, 0.28 wt% Si, 0.003 wt% S, 0.028 wt% P, 1.92 wt% Mn, 0.023 wt% C and Fe. 304L samples were prepared by mechanical polishing using SiC abrasive papers down to a granulometry of 2.5 µm and then electropolished at 40 V for 10 s with a solution of 90% CH_4O and 10% $HClO_4$ at a temperature between 5-10°C.

2.2. Experimental imaging setup and parameters

An Olympus PMG 3 optical microscope coupled with an Olympus DP20 camera has been employed. The ultimate spatial resolution of this microscope is about 0.2 µm and Polarized Light (PL) imaging is also available. PL imaging has been used on Zy-4 samples in order to obtain several images of the same area with varying grain contrasts.

A Tescan MAIA 3 Field Emission Gun SEM (FEGSEM) with a BSE detector has been used for SEM/BSE imaging on 304L samples. Three images were taken for each at -1°, 0° and 1° tilt values, to vary electron channeling conditions and therefore grain contrasts as well.

A Carl Zeiss SUPRA 40 FEGSEM has been used to perform EBSD analyses on Zy-4 samples. It is equipped with a Bruker Quantax system (EBSD e^-Flash^{HR} detector and Esprit 2.1 software). A Tescan FERA 3 equipped with a C-Nano EBSD detector (based on CMOS technology) and the AZtek software package from the Oxford company have been used for EBSD analyses on the 304L samples. For EBSD acquisition, a constant step size of 0.3 and 1 µm has been used for Zy-4 and 304L samples respectively. Non-indexed points were ignored when processing data, as they accounted for only <2% of the measurement grid and were mainly located at GBs. Isolated indexed points are also filtered out with a minimum grain size limit of 5 pixels for Zy-4 and 304L samples, corresponding to a minimum grain size of 1.5 µm and 5 µm respectively.

2.3. Grain boundary extraction with edge detection: image analysis based on grey-scale contrasts

The image analysis process applied for GBs extraction, detect grains and measure their morphological properties based on the same principle for both BSE-SEM and PL-OM micrographs. As shown in figures 1 and 2, a set of images of the same zone exhibiting various intensity levels is used as input data. Only one experimental parameter is modified between images belonging to the same set. In the case of BSE images, tilt angle is varied whereas polarization angle is changed for OM images. All the images associated with an analyzed area are acquired before moving on to the next one. Post-processing method makes use of sharp intensity variations between adjacent grains to detect GBs on each image of the original set. Because intensity of each grain varies between images, some neighbouring grains could exhibit steep contrast variations or not. Hence, some GBs are detected on some images and not on others. The method developed and used in this study aims to take advantage of this by superposing detected GBs of each image, maximizing their detection.

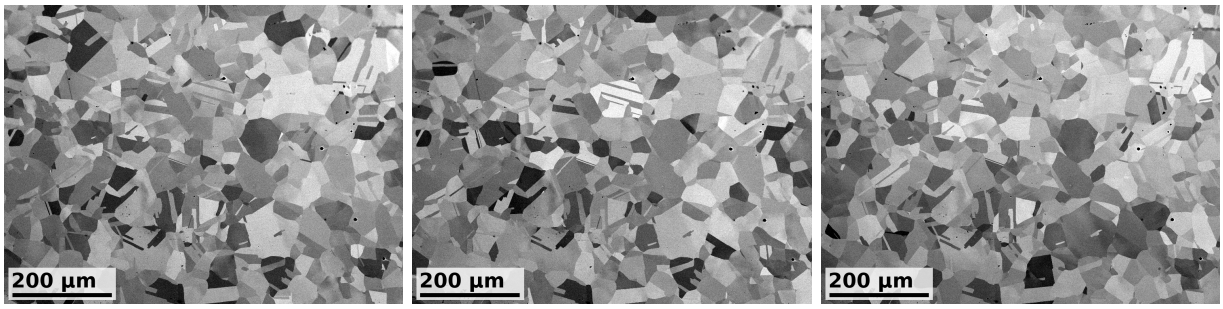

(a) 0° tilt (b) 1° tilt (c) -1° tilt

Figure 1: 304L sample: set of BSE-SEM micrographs. Three tilt angles are used to vary grains contrast.

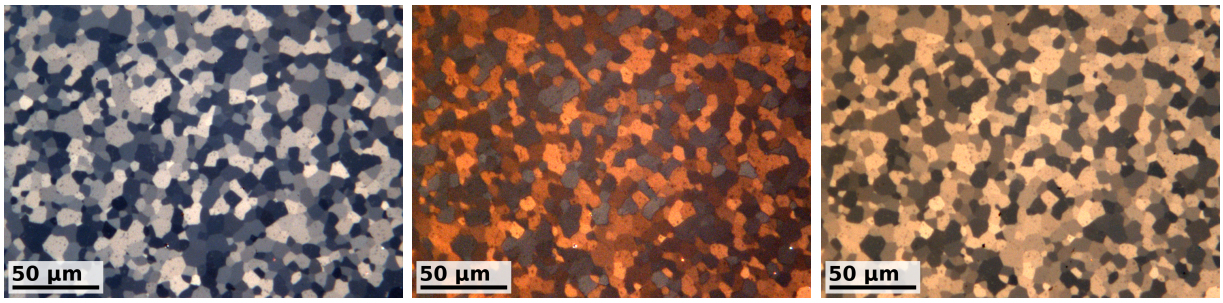

(a) (b) (c)

Figure 2: Zy-4 sample: set of PL-OM micrographs. Three (or more) polarizations are used to vary grain contrast.

An overview of the main steps of the image analysis process is provided on figure 3, as well as intermediate results obtained on PL-OM micrographs of a Zy-4 sample.

If necessary, images are first manually realigned. Considering the two applicative cases presented in this work, limited realignment had to be done. While not being integrated to the actual image analysis procedure, image registration (image alignment algorithms) can be used in order to automate this pre-step. Then, for each image of the analyzed area that presents different local grain contrasts, the following steps (fig. 3) are completed within the Fiji software package [21]:

- Pre-processing. This step consists in adjusting brightness and contrast thanks to a user-defined saturation parameter. Then, a denoising operation is achieved: different denoising algorithms may be used depending on the type of micrographs.
- Detection of GBs. This operation is made using a Sobel edge detector filter, which allows detection of abrupt intensity variations in the image, such as the ones at GBs between two grains with different grey levels. In this step, additional image processing is necessary in order to provide a suitable image for the next processing operation. This includes the use of a mean filter, which prevents over-segmentation later on.

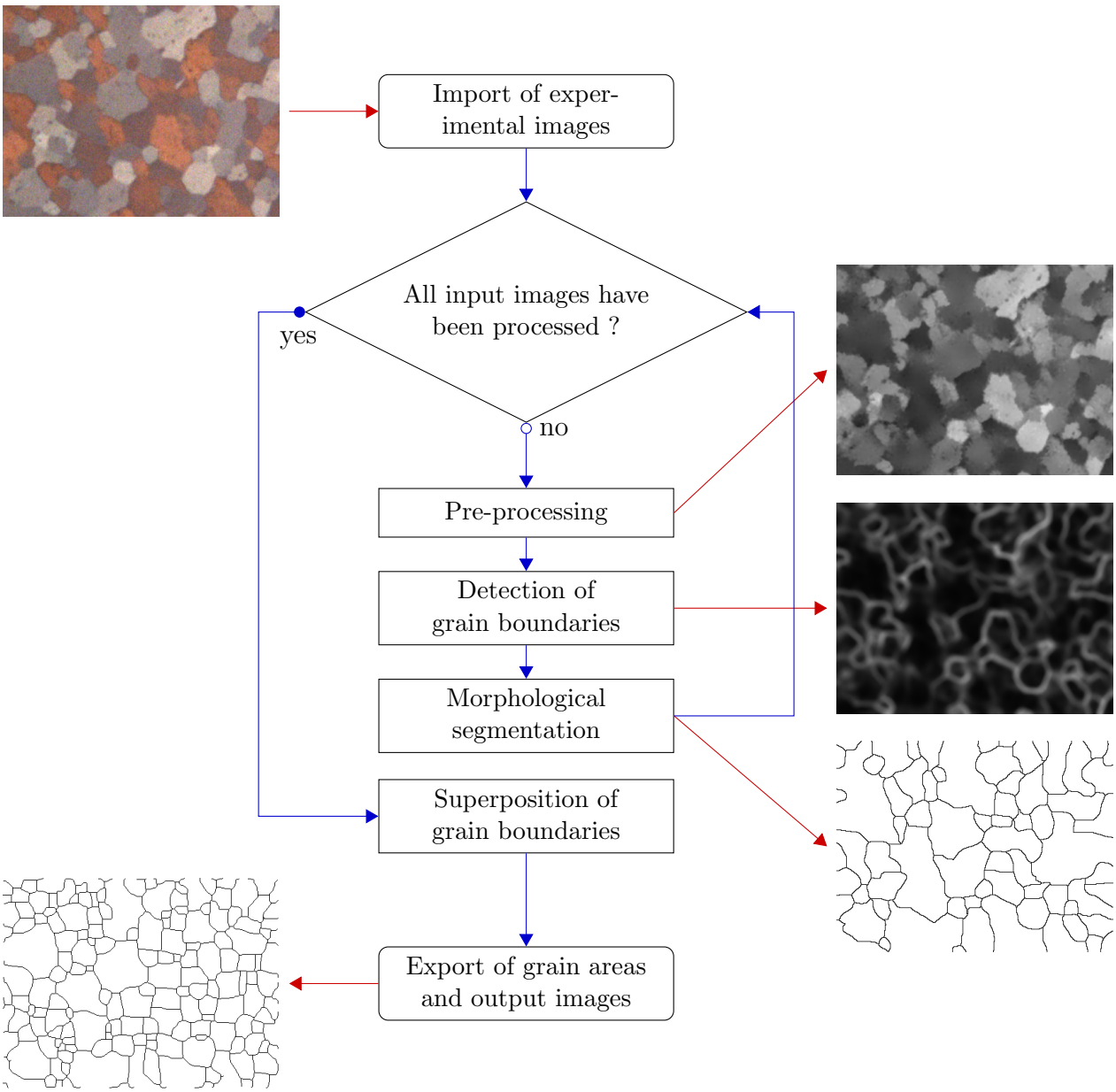

Figure 3: Flow-chart illustrating the main steps of the image analysis procedure. Example images are PL-OM micrographs of a Zy-4 sample.

- Morphological segmentation of grains. Segmentation is performed thanks to the library MorpholibJ [22] and is based on the watershed transform.

After having performed all the operations described above, a binary image is obtained with GBs detected in black and all the remaining parts of the image in white. Once this binary image is obtained for each image of the original set, the resulting images are superposed. The latter is achieved by multiplying all images and performing erosion and dilation oper-

ations to correct and overcome potential slight shifts in the position of the GBs detected on each image. One should note that the latter step could slightly affect the position and morphology of the detected GBs on the final resulting image. Finally, grains are identified and their morphological attributes are measured thanks to the automatic particle counting function built-in Fiji. Cut grains at the edges and corners of the micrographs are not taken into account in those measurements.

Because of differences between images obtained with BSE or OM, minor adaptations have been implemented. Firstly, to standardize the post-processing, a choice was made to only work with grey-scale images. PL-OM micrographs channels are split in order to keep full information and the resulting images are converted into grey-scale ones. Then, the three images, that respectively represent red, green and blue components, are processed one by one. At the end, GBs detected for each channel are superposed and combined into a single image. This operation is achieved thanks to the same procedure as described above: images multiplication (superposition), erosion and dilation. Figure 4 presents both the channel splitting and processing steps. Secondly, since image noise is different depending on the imaging setup, the post-processing has been adapted in each case. For BSE images, the denoising operation in the pre-processing step is achieved thanks to the PureDenoise plugin [23]. For OM images, denoising is achieved using the non-local-means denoising algorithm [24]. The use of these two plugins is convenient as, in both cases, auto-estimation of denoising parameters can be achieved.

2.4. Grain size descriptors

The Equivalent Circle Diameter (ECD), *i.e.* the diameter associated to a disk of same area as the grain, can be calculated for each grain i of area A_i:

$$\mathrm{ECD}_i = 2\sqrt{\frac{A_i}{\pi}} \tag{1}$$

2.4.1. From individual grain data to mean grain size

If individual grain areas can be accessed then several definitions can be used as a mean grain size value:

- Based on the mean area:

$$\bar{A} = \frac{\sum_{i=1}^{N} A_i}{N} = \frac{A_{analyzed}}{N} \tag{2}$$

$$\overline{\mathrm{ECD}}_{\bar{A}} = 2\sqrt{\frac{\bar{A}}{\pi}} \tag{3}$$

$$\mathrm{d}_{\mathrm{ASTM}} = \sqrt{\bar{A}} \tag{4}$$

$$\frac{\overline{\mathrm{ECD}}_{\bar{A}}}{\mathrm{d}_{\mathrm{ASTM}}} = 2\sqrt{\frac{1}{\pi}} \approx 1.28 \tag{5}$$

- Based on the ECD:

$$\overline{\mathrm{ECD}} = \frac{\sum_{i=1}^{n} \mathrm{ECD}_i}{N} \tag{6}$$

A_i and $A_{analyzed}$ being respectively the area of the i$^{\text{th}}$ grain and the analyzed area of the considered domain. N is the number of grains belonging to the analyzed area: domain edge and corner grains are not taken into account.

One can note that a factor of 1.128 (eq. (5)) exists between $\overline{\mathrm{ECD}}_{\bar{A}}$ (eq. (3)) and the mean quadratic diameter (or ASTM diameter) $\mathrm{d_{ASTM}}$ (eq. (4)).

2.4.2. Counting, intercept and intersect methods

Standardized counting methods [10, 25] are based on counting the grains present in the analyzed area ($A_{analyzed}$). A weight is usually applied to truncated grains on the edges and corners of the micrograph, such as [25]:

$$n = n^{interior} + \frac{1}{2} n^{edge} + \frac{1}{4} n^{corner} \tag{7}$$

n being the number of grains in $A_{analyzed}$, superscripts denote interior, edge and corner grains respectively.

A mean grain area can then be computed using eq. (2)). A mean grain size value can then be obtained using eq. (3) or eq. (4).

Considering the intercept and intersect methods [7, 8], a mean intercept/intersect length is obtained. Figure 5a illustrates a 2D microstructure with 960 grains generated using Real-IMotion [26]. As presented on figure 5b grains (intercept method) or GBs (intersect method) are counted along a test line which can either be a circle (as in fig. 5b) or a line. Readers are refered to ASTM [10] and ISO [25] standards and to the works of Hilliard [7] and Abrams [8] for further details.

As for the general counting method presented above, a weight is applied to particular intercept or intersect, such as [25]:

- If n_g is the number of intercepted grains:

$$n_g = n_g^{intercepted} + \frac{1}{2} n_g^{end} + \frac{1}{2} n_g^{tangent} \tag{8}$$

  where superscripts ^{end} and ^{tangent} are associated with the interceptions at the end of the test line (no n_g^{end} is the case of a test circle) and when the test line is tangent to a GB, respectively.

- If n_{gb} is the number of intersected GBs:

- Considering straight test lines:

$$n_{gb} = n_{gb}^{intersected} + n_{gb}^{tangent} + \frac{3}{2} n_{gb}^{triple\ junction} \tag{9}$$

- Considering a circle:

$$n_{gb} = n_{gb}^{intersected} + n_{gb}^{tangent} + 2 \times n_{gb}^{triple\ junction} \tag{10}$$

where superscript ^{tangent} is linked to intersections tangent to the GBs while $^{triple\ junction}$ is associated with the eponymous particular points.

In a similar manner than with the $A_{analyzed}$ of the counting method, the length of the test line L_{test} (or the perimeter of the test circle) is divided by the (weighted) number of intercepted grains / intersected GBs in order to obtain the mean linear length denoted $\bar{l}$:

$$\bar{l} = \frac{L_{test}}{n_g} = \frac{L_{test}}{n_{gb}} \tag{11}$$

2.4.3. Comparison between different MGS definitions

Table 1 summarizes the MGS results obtained on the 2D microstructure presented in figure 5. Different MGS definitions are compared either using the individual grain areas obtained by image analysis or by the standardized counting, intercept and intersect methods (see sections 2.4.1 and 2.4.2 for more details).

Method	Entities	eq. (2) $\bar{A}$ µm^2	eq. (3) $\overline{ECD}_{\bar{A}}$ µm	eq. (4) $\bar{d}_{ASTM}$ µm	eq. (6) $\overline{ECD}$ µm	eq. (11) $\bar{l}$ µm
Individual grain data	854	1286.3	40.5	35.9	35.8	
Counting	960	1406.3	42.3	37.5		
Intercept	70					40.9
Intersect	86					33.3

Table 1: Mean grain size of the 2D microstructure presented in fig. 5 obtained according to different definitions.

All these quantities, likely to be used as MGS values, vary within a range of 21%. Althought every MGS definitions provided in table 1 enables to define a MGS value for the microstructure, a clear statement of which one is used has to be made when the term mean grain size is employed. In the following, if nothing else is specified, the MGS refers to the $\overline{ECD}$ (mean equivalent circle diameter).

2.5. Plots of grain size distributions

Different plots can be used for GS analysis and comparisons purposes. Classical histogram plots provide a graphical representation of the GSD based on a defined number of bins: each bin corresponds to a GS interval and y-axis can either be the number or surface fraction of grains belonging to the GS interval (*cf.* figure 6). In figure 6, the equivalent circle diameter is used to define GS intervals for the x-axis but other GS descriptor can be used instead (*e.g.* grain area). GSDs can be compared if the number of bins remains the same. Under- or overestimating the number of bins can impair the data analysis: figure 7 illustrates that aspect by replotting the ECD vs. surface fraction (fig. 6b - 25 bins) with respectively 10 (fig. 7a) and 100 bins (fig. 7b). With 10 bins, the grain size distribution lacks readability with GS intervals around 10 µm: GS around MGS have surface fraction closed to the last bin whereas with a higher number of bins a clear peak is observed around 90 µm. By underestimating the number of bins, GSD tends to be undersampled and characteristic information of the distribution watered down. On the contrary, oversampled GS data (fig. 7b - 100 bins) might be detrimental as well due to the readability of the histogram.
Rules exist to help identify the optimal number of bins. For instance, one can cite the works of Sturges [27] or Freedman-Diaconis [28] which both provide rules used to find an optimal bin width based on different hypotheses.

Violin plots might be a worthy alternative to histograms because they provide numerous information on the considered data in a synthetic plot. Violin plots are derived from the classical box plots introduced by Tukey in 1977 [29]. The box of the box plot is delimited by the 1st and 3rd quartiles (Q_1 and Q_3) and the whiskers are defined as 1.5× the inter-quartile range ($Q_3 - Q_1$), if points are outside of this range they are considered as outliers and are represented by scatter points. The median (or 2nd quartile - Q_2) is also usually represented. Violin plots [30] considers the whole range of data and uses the Kernel Density Estimation (KDE) to give an insight of the distribution. KDE is a way to estimate the probability density function and is closed to histogram representation with the addition of a smoothing parameter (the bandwidth). This smoothing parameter can be automatically estimated using a defined method, especially in the case of a Gaussian kernel. KDE is used here as a visualization tool to complete classical statistical descriptors available in a box plot. Figure 8 presents the coupled violin and box plots representation that will be used in this work. The `matplotlib` python library has been used (`matplotlib.axes.Axes.violinplot` [31]) with default parameters: 100 points are considered for the gaussian kernel density estimation and the bandwidth parameter is estimated based on Scott's rule [32]. In our coupled violin and box plots representation, box plot is represented in black with Q_1 and Q_3 being the extremities of the box and Q_2, the median, a scatter white point. Whiskers are also plotted with two black points delimiting the extremities of the 1.5× inter-quartile range. The KDE of the violin plot is the semi-transparent colored density trace and minimum, mean and maximum values of the dataset are represented by grey bars.

3. Results

Several analysis techniques have been applied to the two materials. First, a sensitivity study regarding post-processing parameters for EBSD and image analysis techniques is proposed. Two by two comparisons between the different analysis techniques are then provided.

3.1. Zy-4 sample: sensitivity study on post-processing parameters

In this subsection, results obtained on the Zy-4 sample are compared in terms of post-processing parameters. For EBSD orientation data, the effect of the misorientation angle threshold selected for GBs detection is investigated. Regarding PL-OM, two key parameters are under study. While most of the other parameters can be automatically refined, the number of PL images used and the mean filter radius value before the segmentation operation have to be manually found. The number of micrographs have to be optimized to fulfill both a correct estimation of MGS and of GSD and also limited acquisition and analysis time. Regarding the mean filter radius, a strong dependence on the image quality have been observed, an automatic refinement of this parameter is then not straightforward.

3.1.1. EBSD: misorientation angle threshold between grains

Figures 9 and 10a illustrate the effect of misorientation angle threshold on GB networks (fig. 9) and GSD (fig. 10a). In the case of a fully recrystallized and equiaxed microstructure such as the one of the Zy-4 sample, differences are scarce between 5, 10 or 15° misorientation angle thresholds.

Similar conclusions can be drawn from MGS values (*cf.* table 2 and fig. 10b). The lower the misorientation angle, the higher the number of detected grains which tend to slightly increase the number of small grains which in turn decreases the overall mean grain area and associated MGS. $\overline{ECD}$ variation remains under 7% when the misorientation angle threshold is between 5° and 15°.

Technique	Misorientation angle threshold	Grains	eq. (2) $\bar{A}$ µm^2	eq. (3) $\overline{ECD}_{\bar{A}}$ µm	eq. (4) d_{ASTM} µm	eq. (6) $\overline{ECD}$ µm
EBSD	5°	1022	34.7	6.6	5.9	6.0
EBSD	10°	957	36.8	6.8	6.1	6.1
EBSD	15°	856	40.5	7.2	6.4	6.4

Table 2: MGS computed from EBSD individual grain data of the Zy-4 sample (fig. 10) using different misorientation angle threshold values for GB detection.

3.1.2. PL-OM: number of micrographs

Image analysis with PL images relies on color differences in order to differentiate grains. By varying the polarization angle, several images with different contrasts can be obtained.

One of the main processing parameter for PL-OM is the number of PL micrographs because some GBs are poorly contrasted on single images. Figures 11 and 12a provide respectively GB networks and GSD obtained with different numbers of PL images considered.

Table 3 summarizes MGS results regarding the sensitivity study associated with the number of PL images considered. Mean grain sizes tend to stabilize, either considering the $\overline{ECD}$, $\overline{ECD}_{\bar{A}}$ or d_{ASTM}, with respect to the increase of the number of PL micrographs. Figure 12b illustrates graphically this effect on either the mean or median GS or other characteristic statistical quantities. 3 to 4 images seems to be enough in order to obtain both GSD and MGS correct estimations.

Technique	Number of PL images	Grains	eq. (2) $\bar{A}$ µm^2	eq. (3) $\overline{ECD}_{\bar{A}}$ µm	eq. (4) d_{ASTM} µm	eq. (6) $\overline{ECD}$ µm
PL-OM	1	487	56.4	8.5	7.5	7.5
PL-OM	2	651	43.9	7.5	6.6	6.8
PL-OM	4	760	37.4	6.9	6.1	6.2
PL-OM	6	819	35.2	6.7	5.9	6.1

Table 3: MGS computed with individual grain data from PL-OM images of the Zy-4 sample (fig. 12) using different number of PL images.

3.1.3. PL-OM: mean filter parameter for image analysis

In the case of the image analysis post-processing an other key parameter is related to the mean filter used before the segmentation step. As stated in the subsection 2.3, this mean filter parameter (R_m) enables smoothing of the images after the Sobel edge detection which filters a part of the noise and in turn limits any undesired over-segmentation during the following steps. This parameter R_m is the kernel radius in pixels of the mean filter. Here a simple mean filter is used such as for each pixel of the image its value is averaged between itself and its neighbors within R_m.

Figure 14 shows that if the R_m value is too low, extra GB are detected (*cf.* fig. 13) which tend to increase the number fraction of smaller grains and shift toward lower grain sizes the whole GSD (*cf.* fig. 14a). A similar result is obtained with a too high R_m value, processing artefacts arise and might impair GB detection. Intermediate values of R_m (between 6 and 9) seem to provide satisfactory results in the present case. This parameter is clearly dependent on the quality of the used micrographs. On this aspect, a fine tuning of sample preparation and image acquisition setup might be necessary in order to optimize the image analysis procedure.

MGS results (table 4 and violin/box plots - fig. 14b) provide similar conclusions. At first, MGS (and other statistical quantities) tends to increase with increasing R_m until R_m = 6-9 px. The case with R_m = 15 px exhibits a rather different kernel density estimation than

lower R_m values which supports the detrimental effect of mean filter numerical artefacts on GB detection discussed above. Based on these observations, a medium R_m value (R_m = 6 px) is used in the present work.

By increasing R_m values, $\bar{A}$, $\overline{ECD}_{\bar{A}}$ and d_{ASTM} also increase. All these MGS definitions rely on the mean area ($\bar{A}$) so if $\bar{A}$ increases, $\overline{ECD}_{\bar{A}}$ and d_{ASTM} increase as well. But if the ECD of each grain is used to obtain a mean ECD ($\overline{ECD}$) then the results are not as straightforward. For instance, with R_m = 15 px, the $\overline{ECD}$ decreases compared to the one obtained with R_m = 9 px.

Technique	R_m		Entities	eq. (2) $\bar{A}$	eq. (3) $\overline{ECD}_{\bar{A}}$	eq. (4) d_{ASTM}	eq. (6) $\overline{ECD}$
	px	µm		µm^2	µm	µm	µm
PL-OM	3	0.9	966	29.3	6.10	5.41	5.47
PL-OM	6	1.8	760	37.4	6.90	6.12	6.22
PL-OM	9	2.7	651	43.6	7.45	6.60	6.68
PL-OM	15	4.5	580	45.9	7.64	6.77	6.22

Table 4: MGS computed with individual grain data from PL-OM images of the Zy-4 sample (fig. 14) using different values for the R_m mean filter kernel radius for image analysis.

3.2. Zy-4 sample: comparing EBSD and OM with PL imaging

The same area is observed using EBSD and PL-OM considering 15° as the limit value between Low Angle GB (LAGB) and High Angle GB (HAGB) regarding orientation data and up to 6 PL-OM images. Figure 15 illustrates the results obtained with the two techniques.

Table 5 summarizes MGS values computed using different definitions. In the case of a relatively homogeneous and equiaxed microstructure such as the one of the Zy-4 considered in this work, EBSD and PL-OM imaging provide similar MGS results considering individual grain data. Counting and intercept methods are able to give good estimation of the MGS even if these methods tend to slightly over-estimate MGS values (around 10% of difference) compared to individual grain data. The violin plot in figure 15e shows very comparable results between EBSD and PL-OM micrographs. Grain size information either regarding mean or median values are closed to each other. The overall grain size range is slightly higher considering EBSD but GSD are mainly defined on a similar ECD range.

3.3. 304L sample: comparing EBSD and BSE imaging

This 304L sample has been prepared for BSE and EBSD observations, *i.e.* with a final electro-polishing step. Comparison is then performed on the same area considering a 5° misorientation angle threshold for GBs detection from EBSD data and 3 micrographs (*i.e.* one -1°, 0°, 1° tilt angles series) for the BSE based method. Results are presented in figure 16.

Technique	Method	Entities	eq. (2) $\bar{A}$ µm^2	eq. (3) $\overline{ECD}_{\bar{A}}$ µm	eq. (4) d_{ASTM} µm	eq. (6) $\overline{ECD}$ µm	eq. (11) $\bar{l}$ µm
EBSD	Ind. grain data	856	40.5	7.18	6.37	6.40	
OM+PL	Ind. grain data	734	39.0	7.05	6.25	6.35	
OM+PL	Counting	805	49.9	7.97	7.06		
OM+PL	Intercept	63.5					7.05

Table 5: Zy-4 sample (analyzed area: 229 µm × 168 µm): MGS computed from EBSD and PL-OM micrographs (fig. 15) obtained by different procedures.

Figures 16a and 16b enable a visual comparison between the two techniques. One can note a slight distortion of the observation area in the case of EBSD data compared to BSE imaging: this can be attributed to some remaining distortion induced by inaccuracy in the correction of the 70° tilt (*i.e.* the classical configuration for EBSD analysis). Two main aspects have to be taken into account:

- Image distortion may not be perfectly corrected (especially for large view fields) by the SEM and the EBSD system.
- Sample positioning in the sample holder is never perfect: even a slight angle fraction is likely ever existing between the sample surface and the horizontal when the stage tilt is 0°. As a consequence the classical EBSD configuration (analyzed surface 70° tilted) may not be strictly respected. The latter can also have a detrimental influence on the image distortion correction.

These aspects are described, amongst other sources of image distortions in the SEM, with further details by Nolze in [33]. In our particular case, the two points presented above are likely to explain the differences observed between BSE and EBSD.

For the sake of strict comparison between the acquisition methods no correction linked to these distortions has been performed in the present work. A direct comparison between the raw data of each technique is then achieved.

Twin boundaries (especially Σ3 ones) are well detected in the case of EBSD. With crystallographic orientation data, twin boundaries can either be considered as special GBs or filtered out based on their misorientation (here, for FCC 304L, 60±5° about <111>). In the case of BSE imaging, twin boundaries cannot be distinguished from other GBs based on their misorientation. Twin detection is then not as accurate and often leads to an altered description of the local grain structure. The twin boundary highlighted by an arrow in the two figures illustrates that aspect. One may note that only using a misorientation criterion can impair the EBSD grain size measurements associated with twin boundaries. Wright and Larsen [34] showed that to only consider coherent twin boundaries the boundary plane has to be aligned with the considered twinning plane. By doing so, only coherent twins can be filtered out for grain size measurements. In the present work, only the misorientation

criterion has been used which results in no distinction between coherent and incoherent twin boundaries.
Figures 16c and 16d show similar results regarding GSD if Σ3 twin boundaries are considered as GBs between EBSD and BSE analyses either considering number or surface fraction as y-axis. As already stated, BSE image analysis procedure tends to over estimate small grains especially in areas where contrasts are blurry. Results in terms of GSD deviate in the case of EBSD with filtered out twin boundaries: the whole distribution is shifted toward higher grain size values.

Table 6 provides mean grain size results for the considered EBSD and BSE data. Considering individual grain data, BSE and EBSD give similar results if Σ3 grain boundaries are taken into account. The deviation already observed on GSD between EBSD data with or without Σ3 GB is also noticeable on MGS with a difference of around 58% regarding the $\overline{ECD}$. BSE imaging with image analysis post-treatment does not enable an automatic distinction between classical and Σ3 GB. Figure 16e clearly highlights this effect on statistical quantities and on the KDE: if Σ3 GB are filtered with EBSD data, the KDE is wider and mean / median GS is higher than in the case of EBSD with Σ3 GB. BSE micrographs tend to give an intermediate result: the KDE is not as wide as in the case of EBSD without Σ3 GB but a part of these boundaries is not detected which results in a lower MGS. EBSD with Σ3 GB and BSE images present a similar inter-quartile range but mean / median GS is lower in the case of EBSD data. The latter proves to be more reliable regarding Σ3 GB detection than image analysis on BSE micrographs.

Material	Method	Entities	eq. (2) $\bar{A}$ µm^2	eq. (3) $\overline{ECD}_{\bar{A}}$ µm	eq. (4) d_{ASTM} µm	eq. (6) $\overline{ECD}$ µm	eq. (11) $\bar{l}$ µm
EBSD w Σ3	Ind. grain data	1102	563	26.8	23.7	22.2	
EBSD wo Σ3	Ind. grain data	253	2592	57.4	50.9	48.8	
BSE	Ind. grain data	600	580	27.2	24.1	22.7	
BSE	Counting	639	603	27.7	24.6		
BSE	Intercept	51					31.7

Table 6: 304L sample (analyzed area: 984 µm × 739 µm): MGS computed from EBSD and BSE imaging (fig. 16) obtained by different procedures.

4. Discussion

Regarding MGS, definitions relying on individual grain data enable an estimation of MGS with a limited influence of user-dependent biases. Other statistical descriptors may also be derived from individual grain data such as the standard deviation or the median grain size. The other standardized methods (counting and intercept/intersect ones) provide valuable results but may be proned to both user perception and microstructural heterogeneities. In

particular, these techniques may not be relevant in the case of non-equiaxed microstructures or multi-modal GSD. In the cases investigated in the present work, the intercept method tends to over-estimate MGS.

Grey-scale imaging either using BSE-SEM or PL-OM micrographs proved to be suitable in order to obtain accurate information about GSD in metallic alloys. Sample preparation time remains similar to the one for EBSD but acquisition time is reduced and larger areas might be considered. With grey-scale micrographs and image analysis, one can increase the number of observation areas and in turn enhance the statistical representativity of the grain size measurements. The latter is particularly suitable in the case of large grain microstructure for which EBSD may become irrelevant regarding the acquisition time.
In order to further discuss time consideration, table 7 presents the typical acquisition and post-processing times for the different techniques and for the 2 materials used in this work. Post-processing parameters for image analysis have to be refined for a particular material (one set of parameters per preparation/acquisition technique). The latter only has to be done for the first sample of a serie. A maximum of 30 min is required for this parameters refinement step. Considering the worst case scenario with only one sample to analyze, BSE-SEM and PL-OM associated with image analysis remains about 3 and 7 times faster than EBSD analysis on the same area, respectively.

(a) 304L – $A_{analyzed}$ = 984 µm × 739 µm

Technique	Acquisition min	Post-processing min
EBSD	120	5
BSE-SEM	10	(30) + 1

(b) Zy-4 – $A_{analyzed}$ = 229 µm × 168 µm

Technique	Acquisition min	Post-processing min
EBSD	240	5
PL-OM	3	(30) + 1

Table 7: Acquisition and post-processing times for different microscopy techniques: for (a) 304L and (b) Zy-4. Times presented here have been obtained considering the observation areas presented in sections 3.2 (Zy-4) and 3.3 (304L) using acquisition parameters, microscopes and the post-processing procedure described in sections 2.2 and 2.3.

The previous paragraph illustrates that some techniques may be more suitable for certain materials with respect to GSD evaluation. Other considerations than time should also be taken into account. Compared to image analysis results, EBSD orientation mapping, while being usually slower regarding acquisition, provide numerous other information alongside with GS measurements. Local crystallographic orientations may be used to investigate material texture, to exhibit intraganular misorientations, for subgrains identification or GBs classification... Many information that cannot be accessed, at that time, only using image analysis on grey-scale micrographs. The choice of the analysis technique has to be relevant taking into account the following points:

- what microstructural information need to be extracted ? GS measurements (MGS, GSD), crystallographic orientation, chemical composition, phase identification, ...

- what is the necessary view field for statistical representativity ?
- is there any constraints regarding sample preparation ? (*e.g.* oxydation may be opportune for OM but detrimental for SEM observations)
- is the technique suitable for the considered material ? (*e.g.* OM may be advantageous over SEM for non-conductive materials)

Regarding image analysis, PL-OM or SEM-BSE micrographs may become limited, in particular in the case of heavily twinned or deformed microstructures. Figure 17 shows EBSD band-contrast maps obtained on the 304L sample considered in this work. Twin boundaries ($\Sigma 3$) are detected considering a misorientation of $60 \pm 5^{\circ}$ around the <111> axis. In this particular case, the microstructure is composed of more than 1300 twins which have a non-negligible impact on GSD and MGS. Without any orientation data, the filtering of twin GB may not be as efficient and may require extra post-processing steps using grey-scale images.
Other problems may arise on deformed materials: especially over-segmentation due to local intragranular orientation variations. Figure 18 highlights this problematic with a BSE-SEM micrograph of a 316L austenitic stainless steel after a hot deformation ($\varepsilon \approx 0.65$) at 1000°C and a strain rate of 0.01 s^{-1}. Again, without further processing of the micrographs, the actual procedure cannot deal with highly strain-hardened microstructure for accurate GSD estimations.

5. Conclusions

An image analysis procedure based on grey-scale contrast images has been detailed and confronted to EBSD orientation data considering both GSD and MGS. The following points constitute the main conclusions of this work:

- Independently of the microscopy technique employed for grey-scale imaging, the acquisition time of raw data is decreased compared to the one inherent to EBSD analysis. SEM-BSE or PL-OM micrographs have been used successfully for image analysis and both provide reliable individual grain data.
- Using multiple micrographs with varying crystallographic orientation contrasts improves GSD evaluation by image analysis compared to using only one image of the analyzed area.
- If twin boundaries do not require to be filtered for grain size measurements, the image analysis methodology introduced in this work has proven to provide accurate results, especially regarding GSD estimation.
- In terms of MGS evaluation, the use of individual grain areas limits user-dependent approximations and provide a good statistical representativity compared to more conventional methods based on entities counting.

A sensitivity study of several key parameters for both EBSD and grey-scale image analysis has been performed to optimize the processing procedures. The following points may serve as guidelines for GS measurements considering the techniques used in this work:

- The effect of HAGB threshold value on EBSD GS measurements appears to be rather limited in the case of a fully recrystallized sample.
- The number of images required for valuable GSD estimation based on the PL-OM or the BSE-SEM procedure is about 3 to 4 if sufficient crystallographic orientation contrasts exist between the different micrographs.
- The mean filter kernel radius R_m should be defined in order to limit image noise influence on GBs detection by the segmentation algorithm. This kernel radius depends mainly on the micrograph image quality: too small radii may not filter enough noise resulting in over-segmentation while too big radii may lead to a loss of microstructural information.

Regarding image analysis a semi-automatic Fiji/ImageJ macro has been written. The latter still needs to be validated and confronted to other metallic alloys and grey-scale images acquisition techniques but was successfully used to obtain the results presented here. Improvements are especially expected for highly twinned or deformed material regarding image analysis post-processing. For twin boundaries, a morphological filtering based on their particular geometrical shape is under study. The case of deformed samples is more challenging. For these samples a strategy based on a kernel average associated with pixels grey-scale level is currently investigated. The latter could enable an estimation of the fraction of strain hardened grains in the microstructure (or, in other words, open the road to recrystallized fraction estimation) with an image analysis procedure.

Aknowledgements

This work has been supported by ArcelorMittal, Ascometal, Aubert & Duval, CEA, Framatome, Safran, Timet, Constellium and Transvalor companies and the ANR through the DIGIMU consortium – French industrial Chair (Grant No. ANR-16-CHIN-0001). Special thanks are due to S. Jacomet, C. Collin and G. Fiorucci for their respective help on microscopy, samples preparation and heat treatments. The authors also thank P. Barberis and O. Calonne (Framatome) for reviewing the preprint version of this article.

Declaration of competing interest

The authors declare that they have no known competing financial interests or personal relationships that could have appeared to influence the work reported in this paper.

Data availability

The raw/processed data required to reproduce these findings cannot be shared at this time as the data also forms part of an ongoing study.

References

[1] E.O. Hall. The deformation and ageing of mild steel: III discussion of results. *Proc. Phys. Soc. Section B*, 64(9):747–753, 1951.

[2] N.J. Petch. The cleavage strength of polycrystals. *J. Iron Steel Inst.*, 173:25–27, 1953.

[3] B. Raeisinia and C.W. Sinclair. A representative grain size for the mechanical response of polycrystals. *Mater. Sci. Engng A*, 525:78–82, 2009.

[4] S.A. Saltykov. *Stereology: proceedings of the second international congress for stereology*, chapter The determination of the size distribution of particles in an opaque material from a measurement of the size distribution of their sections, pages 163–173. Springer-Verlag New York Inc., 1967.

[5] E.E. Underwood. *Quantitative stereology*. Addison-Wesley Publ. Co., Reading, Massachusetts, 1970.

[6] J.C. Tucker, L.H. Chan, G.S. Rohrer, M.A. Groeber, and A.D. Rollett. Comparison of grain size distributions in a Ni-based superalloy in three and two dimensions using the Saltykov method. *Scripta Mater.*, 66:554–557, 2012.

[7] J.E. Hilliard. Estimating grain size by the intercept method. *Metal Progress*, 85:99–102, 1964.

[8] H. Abrams. Grain size measurement by the intercept method. *Metallography*, 4:59–78, 1971.

[9] A. Bowles, K. Nogita, M. Dargusch, C. Davidson, and J. Griffiths. Grain size measurements in Mg-Al high pressure die castings using electron back-scattered diffraction (EBSD). *Mater. Trans.*, 45(11):3114–3119, 2004.

[10] ASTM E112 - 96 (2004). Standard test methods for determining average grain size, 2004. ASTM International, United States.

[11] R. Quey, P.R. Dawson, and F. Barbe. Large-scale 3D random polycrystals for the finite element method: generation, meshing and remeshing. *Comput. Meth. Appl. Mech. Engng*, 200(17-20):1729–1745, 2011.

[12] K. Hitti, P. Laure, T. Coupez, L. Silva, and M. Bernacki. Precise generation of complex statistical Representative Volume Elements (RVEs) in a finite element context. *Comput. Mater. Sci.*, 61:224–238, 2012.

[13] L. Garca de la Cruz, M. Martinez, C. Keller, and E. Hug. Achieving good tensile properties in ultrafine grained nickel by spark plasma sintering. *Mater. Sci. Engng A*, 772:138770, 2020.

[14] A. Nicolaÿ, J.M. Franchet, J. Cormier, H. Mansour, M. De Graef, A. Seret, and N. Bozzolo. Discrimination of dynamically and post-dynamically recrystallized grains based on EBSD data: application to Inconel 718. *J. Microsc.*, 273(2):135–147, 2019.

[15] F.J. Humphreys. Quantitative metallography by electron backscattered diffraction. *J. Microsc.*, 195(3):170–185, 1999.

[16] F.J. Humphreys. Review – grain and subgrain characterization by electron backscatter diffraction. *J. Mater. Sci.*, 36:3833–3854, 2001.

[17] S.I. Wright. A parametric study of electron backscatter diffraction based grain size measurements. *Prakt. Metallogr.*, 47(1):16–33, 2010.

[18] A.P. Day and T.E. Quested. A comparison of grain imaging and measurement using horizontal orientation and colour orientation contrast imaging, electron backscatter pattern and optical methods. *J. Microsc.*, 195(3):186–196, 1999.

[19] C. Langlois, T. Douillard, H. Yuan, N.P. Blanchard, A. Descamps-Mandine, B. Van de Moortèle, C. Rigotti, and T. Epicier. Crystal orientation mapping via ion channeling: an alternative to EBSD. *Ultramicroscopy*, 157:65–72, 2015.

[20] C. Lafond, T. Douillard, P. Cazottes, P. Steyer, and C. Langlois. Electron CHanneling ORientation Determination (eCHORD): an original approach to crystalline orientation mapping. *Ultramicroscopy*, 186:146–149, 2018.

[21] J. Schindelin, I. Arganda-Carreras, E. Frise, V. Kaynig, M. Longair, T. Pietzsch, S. Preibisch, C. Rueden, S. Saalfeld, B. Schmid, J.-Y. Tinevez, D.J. White, V. Hartenstein, K. Eliceiri, P. Tomancak, and A. Cardona. Fiji: an open-source platform for biological-image analysis. *Nat. Methods*, 9:676–682, 2012.

[22] D. Legland, I. Arganda-Carreras, and P. Andrey. MorphoLibJ: integrated library and plugins for mathematical morphology with ImageJ. *Bioinformatics*, 32(22):3532–3534, 07 2016.

[23] F. Luisier, C. Vonesch, T. Blu, and M. Unser. Fast interscale wavelet denoising of poisson-corrupted images. *Signal Processing*, 90:415–427, 2010.

[24] A. Buades, B. Coll, and J.M. Morel. Non-local means denoising. *Image Processing On Line*, 1:208–212, 2011.

[25] EN ISO 643:2012 (F). Aciers – Détermination micrographique de la grosseur de grain apparente, 2012. International Organization for Standardization.

[26] S. Florez, K. Alvarado, D. Pino Muñoz, and M. Bernacki. A novel highly efficient lagrangian model for massively multidomain simulation applied to microstructural evolutions. *Comput. Meth. Appl. Mech. Engng*, 367:113107, 2020.

[27] H.A. Sturges. The choice of a class interval. *Journal of the American Statistical Association*, 21(153):65–66, 1926.

[28] D. Freedman and P. Diaconis. On the histogram as a density estimator: L^2 theory. *Zeitschrift fr Wahrscheinlichkeitstheorie und Verwandte Gebiete*, 57(4):453–476, 1981.

[29] J.W. Tukey. *Exploratory Data Analysis*. Addison-Wesley Publ. Co., Reading, Massachusetts, 1977.

[30] J.L. Hintze and R.D. Nelson. Violin plots: A box plot-density trace synergism. *The American Statistician*, 52(2):181–184, 1998.

[31] Matplotlib. Violinplot. https://matplotlib.org/3.3.1/api/_as_gen/matplotlib.axes.Axes.violinplot.html?highlight=violin%20plot#matplotlib.axes.Axes.violinplot, Consulted: 2020.09.01.

[32] D.W. Scott. *Multivariate Density Estimation: Theory, Practice, and Visualization*. John Wiley & Sons, New York, Chicester, 1992.

[33] G. Nolze. Image distortions in SEM and their influences on EBSD measurements. *Ultramicroscopy*, 107(2):172–183, 2007.

[34] S.I. Wright and R.J. Larsen. Extracting twins from orientation imaging microscopy scan data. *J. Microsc.*, 205(3):245–252, 2002.

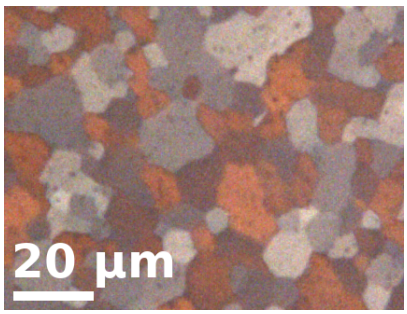

(a) Initial micrograph

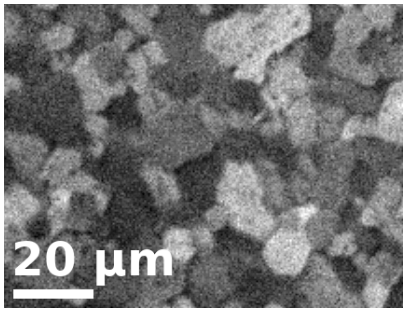

(b) Red

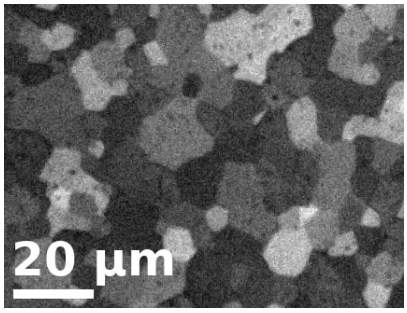

(c) Green

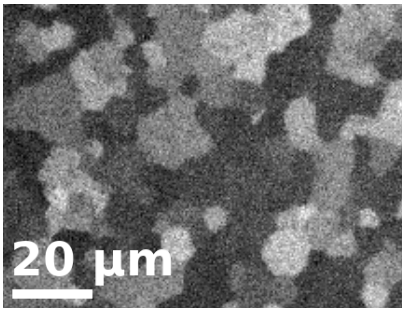

(d) Blue

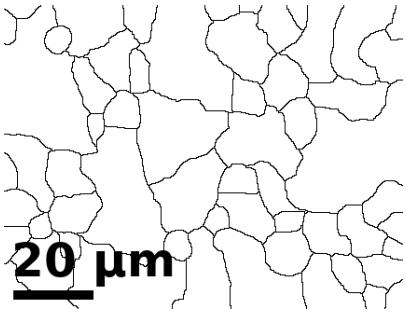

(e) Red

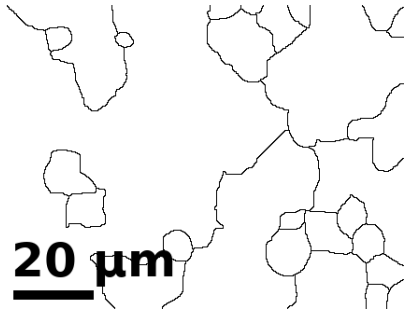

(f) Green

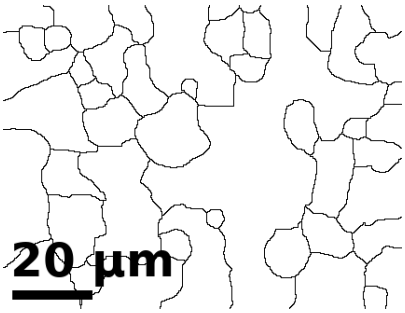

(g) Blue

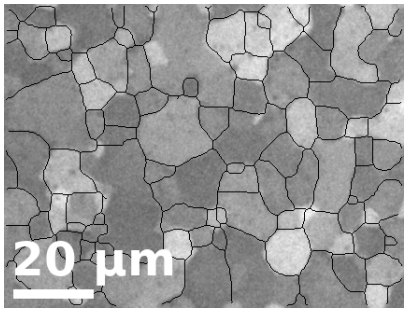

(h) Final image

Figure 4: Selected steps from image analysis procedure for PL-OM micrographs. (a) Initial PL-OM image, (b, c, d) splitting of the three RGB channels and conversion to grey-scale images, each image is then treated (denoising) and (e, f, g) give the resulting GB network for each image after edge detection, (h) Final image after the sum of the three previous GB networks. On this final image, the grey-scale initial image has been superimposed for visual comparison.

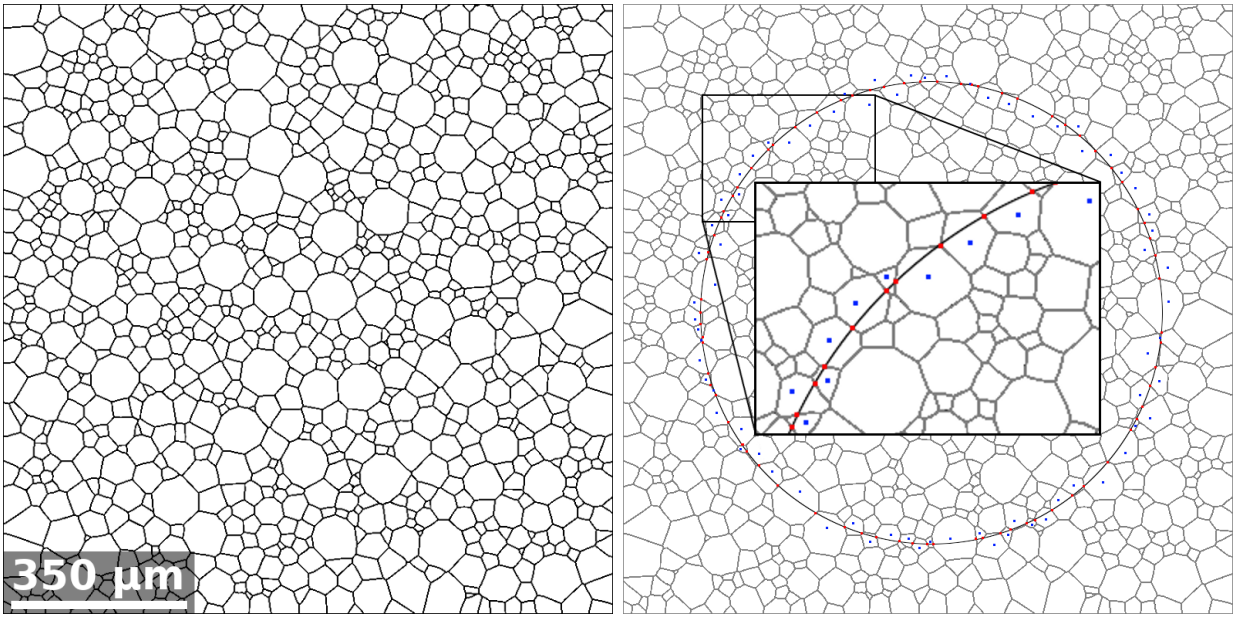

(a) (b)

Figure 5: (a) 2D microstructure with 960 grains (generated with RealIMotion [26]) and (b) circle and counting points used for intercept/intersect procedures to evaluate $\bar{l}$.

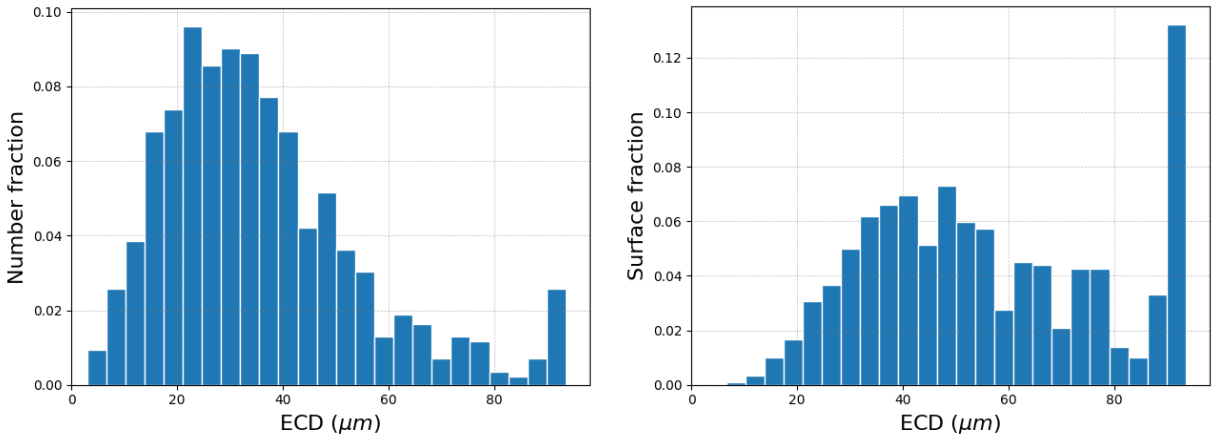

(a) (b)

Figure 6: GSDs considering the equivalent circle diameters (ECD). GS are plotted regarding (a) number or (b) surface fractions.

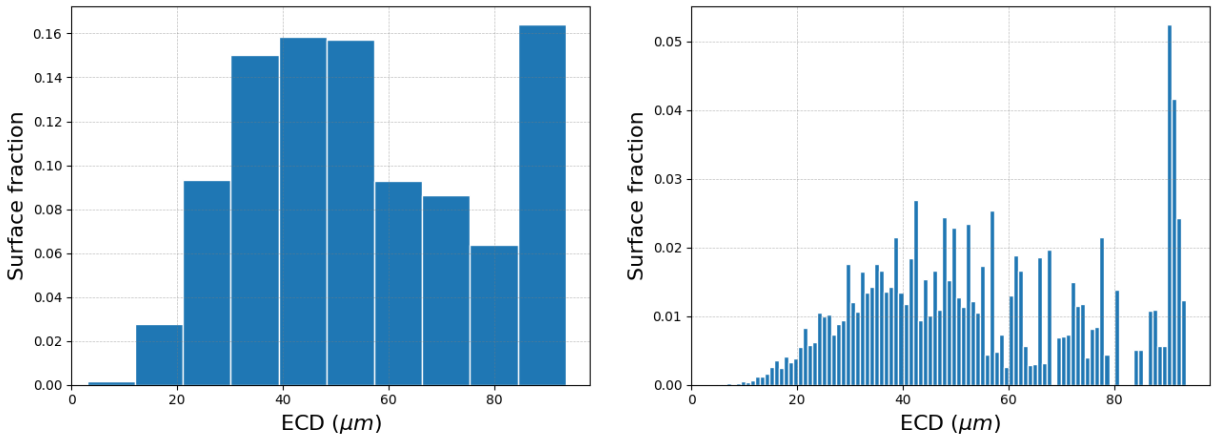

(a) (b)

Figure 7: GSDs considering the equivalent circle diameters (ECD) versus surface fraction. Influence of the number of bins: (a) 10 and (b) 100 bins.

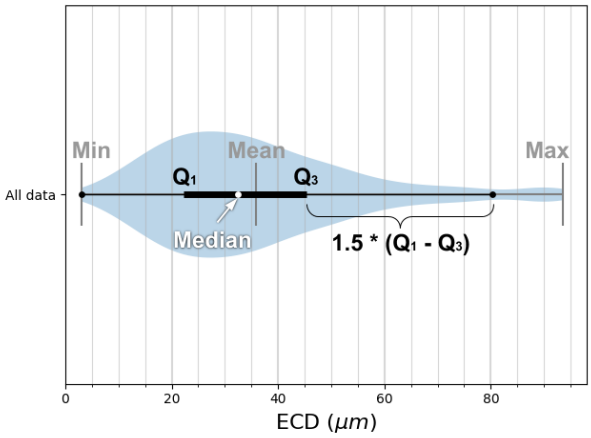

Figure 8: Coupled violin and box plots from the grain size data extracted by image analysis from the microstructure presented figure 5.

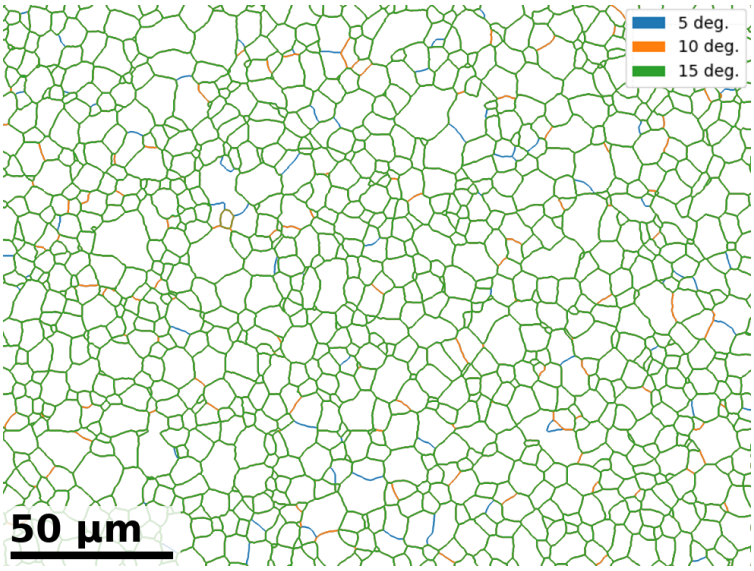

Figure 9: GB networks of the Zy-4 sample for different EBSD GB misorientation threshold (5°, 10° or 15°).

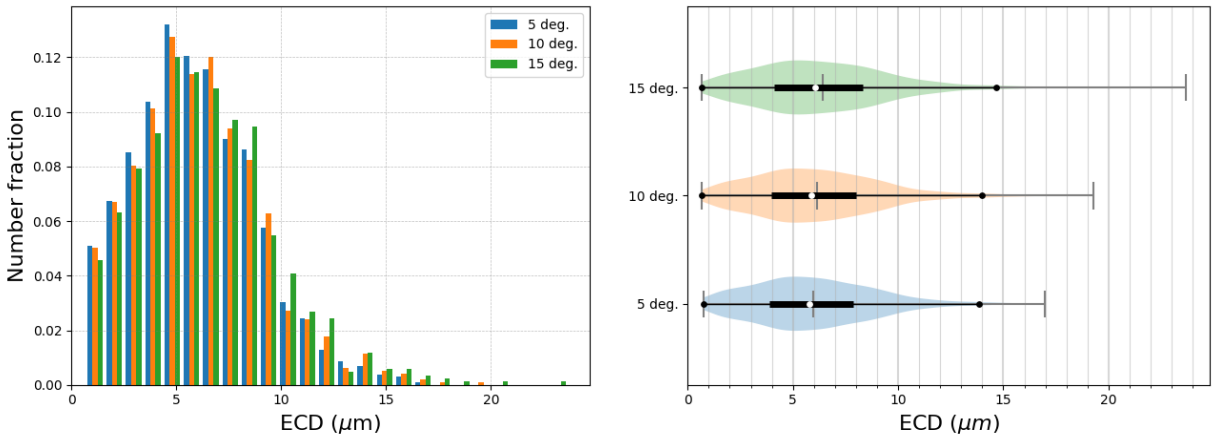

(a) (b)

Figure 10: Parameters sensitivity analysis: EBSD GB misorientation threshold (5°, 10° or 15°) on the Zy-4 sample. (a) GSDs and (b) violin plots.

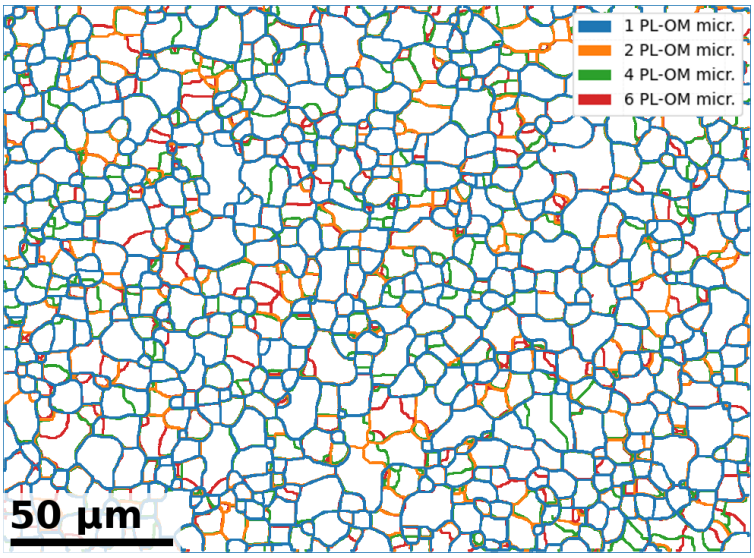

Figure 11: GB networks for different number of PL images used for OM image analysis (1, 2, 4 or 6 images) on the Zy-4 sample.

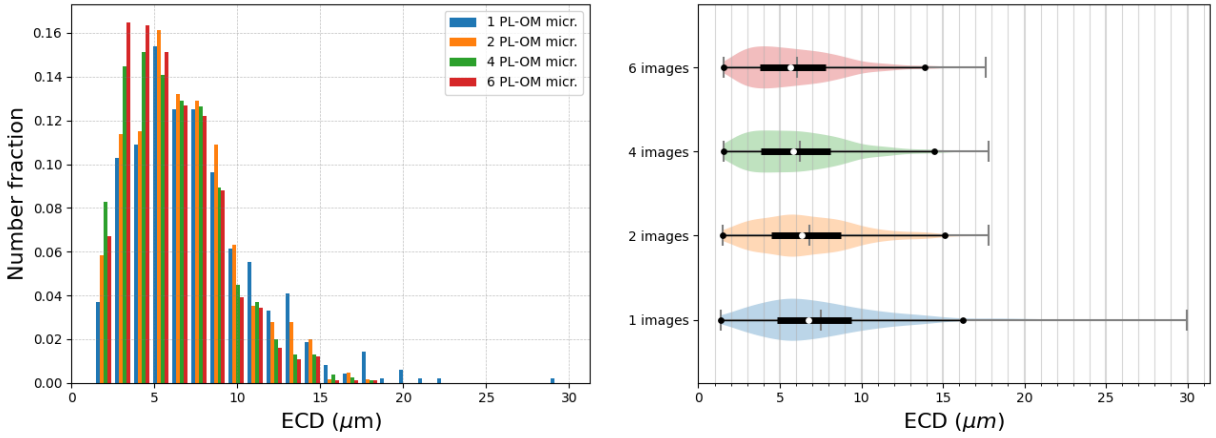

(a) (b)

Figure 12: Parameters sensitivity analysis: number of PL images used for OM image analysis (1, 2, 4 or 6 images) on the Zy-4 sample. (a) GSDs and (b) violin plots.

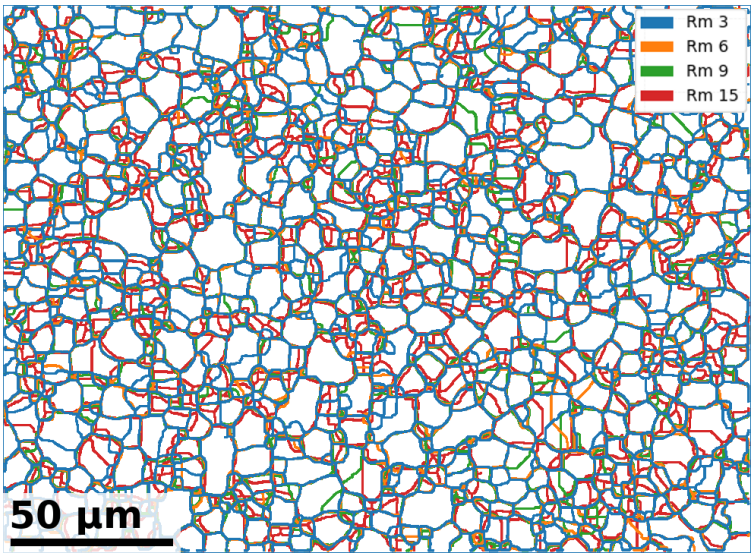

Figure 13: GB networks for different value of the R_m mean filter parameter used for OM image analysis (R_m = 3, 6, 9 or 15) on the Zy-4 sample.

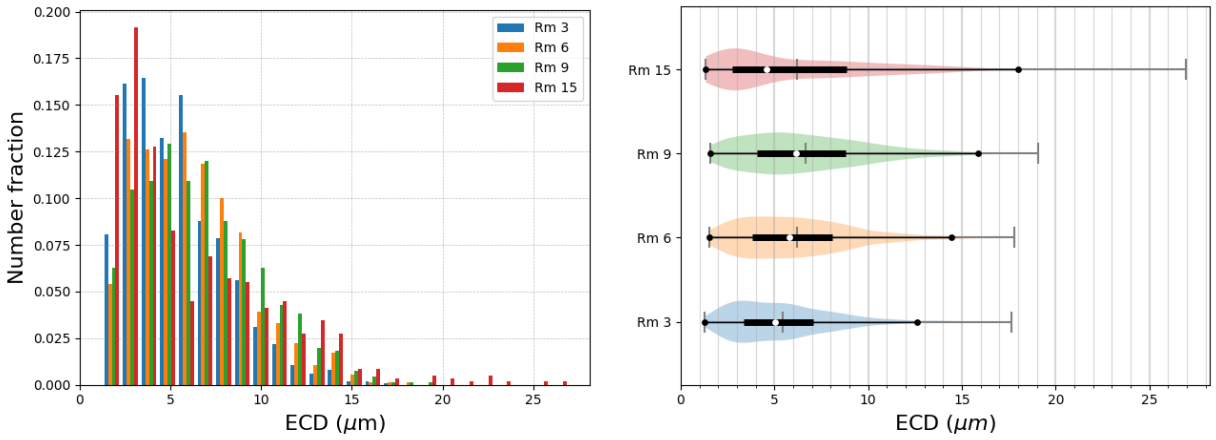

(a) (b)

Figure 14: Parameters sensitivity analysis: value of the R_m mean filter parameter used for OM image analysis (R_m = 3, 6, 9 or 15 px) on the Zy-4 sample. (a) GSDs and (b) violin plots.

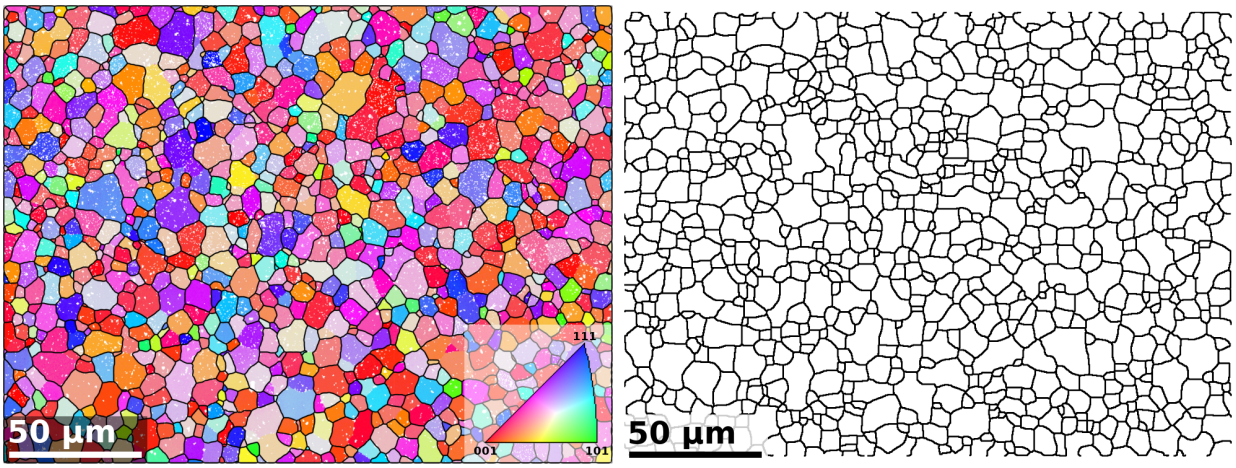

(a) (b)

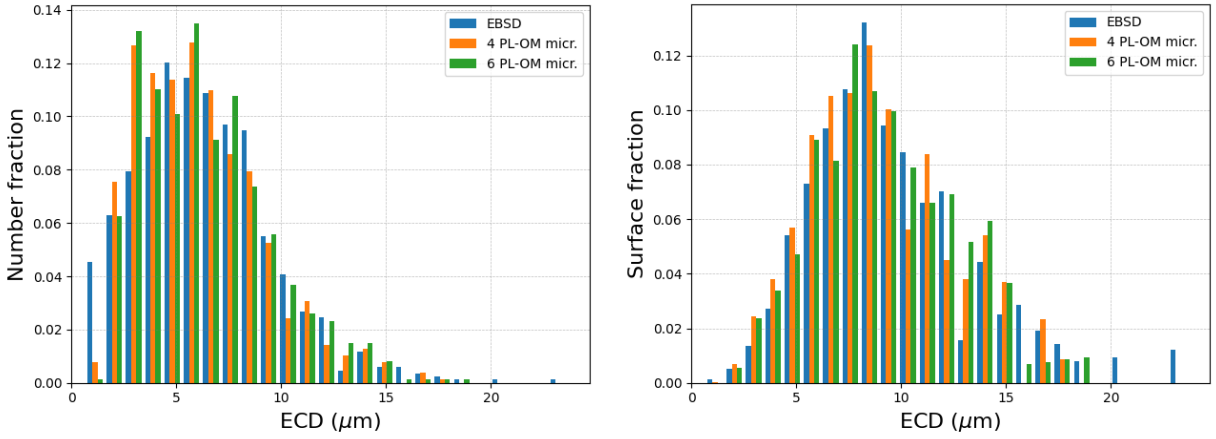

(c) (d)

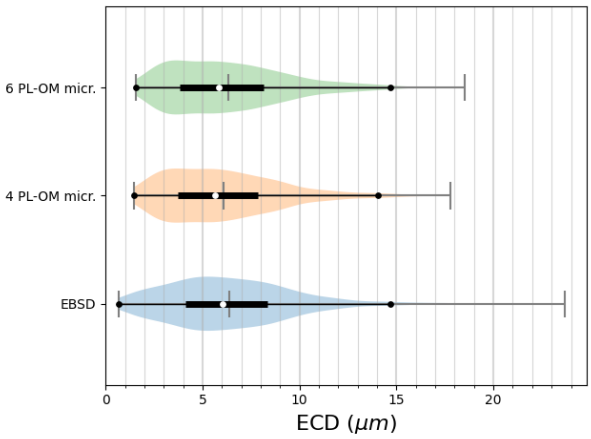

(e)

Figure 15: Zy-4 sample: comparisons between (a) EBSD orientation map and (b) PL-OM contrast imaging with image analysis post-treatment. (c) and (d) provide the GSDs (c) by number and (d) by surface fraction extracted using EBSD and image analyses. The associated violin and box plots are provided in (e).

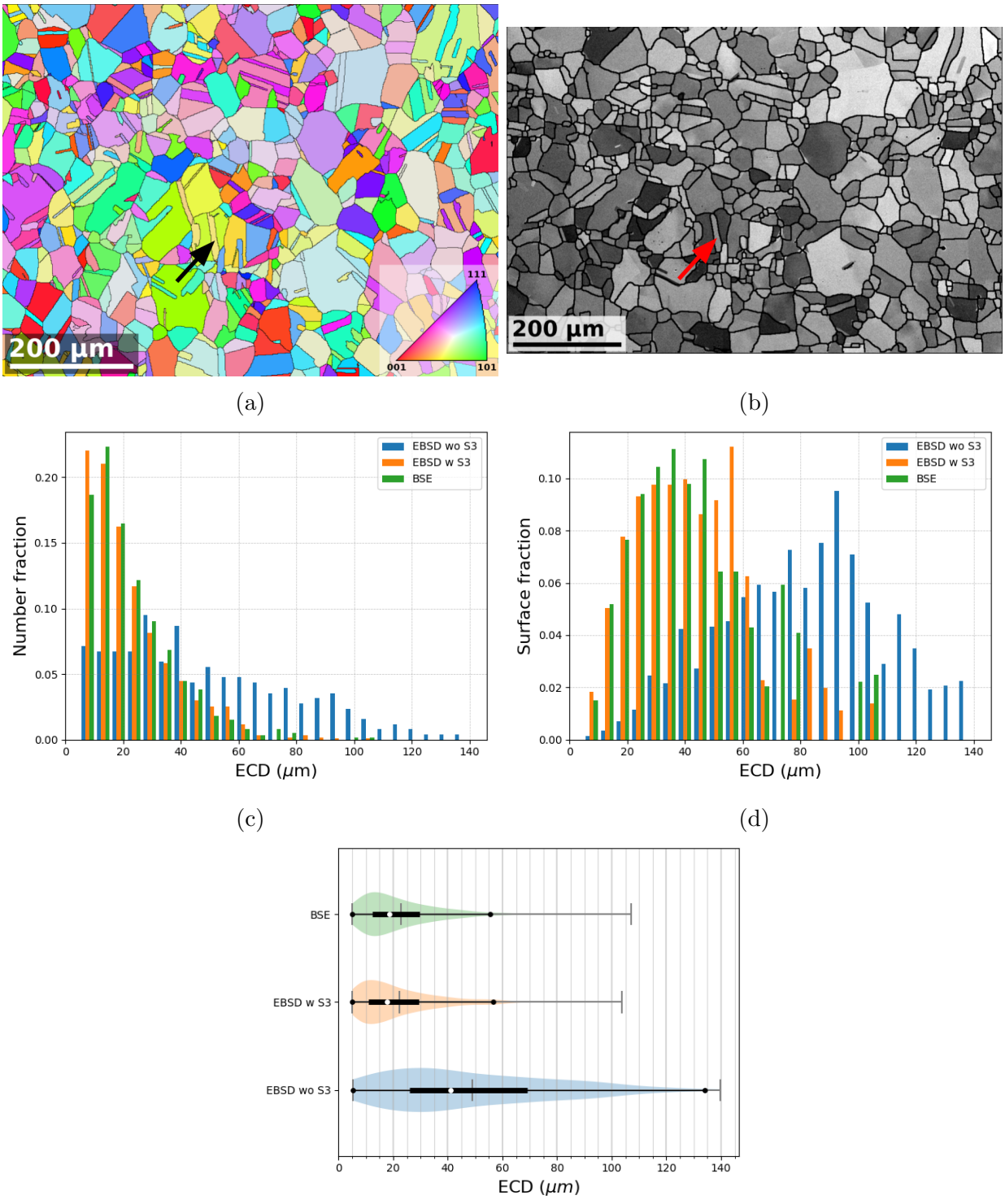

Figure 16: 304L sample: comparisons between (a) EBSD orientation map and (b) BSE contrast imaging with image analysis post-processing. (c) and (d) provide the GSDs (c) by number and (d) by surface fraction extracted using EBSD and image analyses on BSE contrast images. The associated violin and box plots are provided in (e).

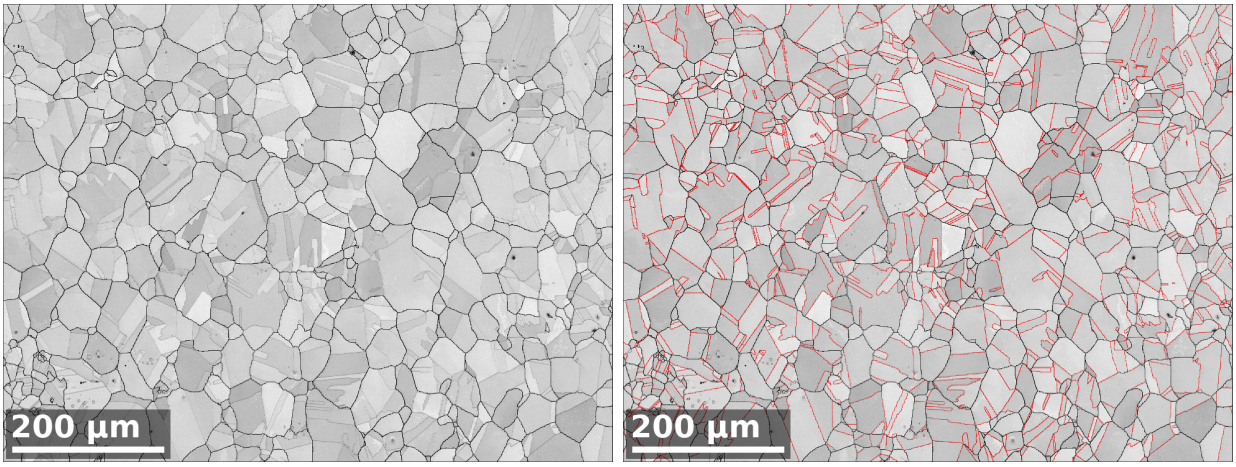

(a) (b)

Figure 17: EBSD band-contrast images obtained on the same 304L sample than in figure 16: (a) without considering twin boundaries ($\Sigma 3$) and (b) with twin boundaries highlighted in red. A misorientation angle threshold of 5° is considered for grain boundaries detection while $\Sigma 3$ twin boundaries are detected considering a disorientation angle of 60±5° around the <111> axis.

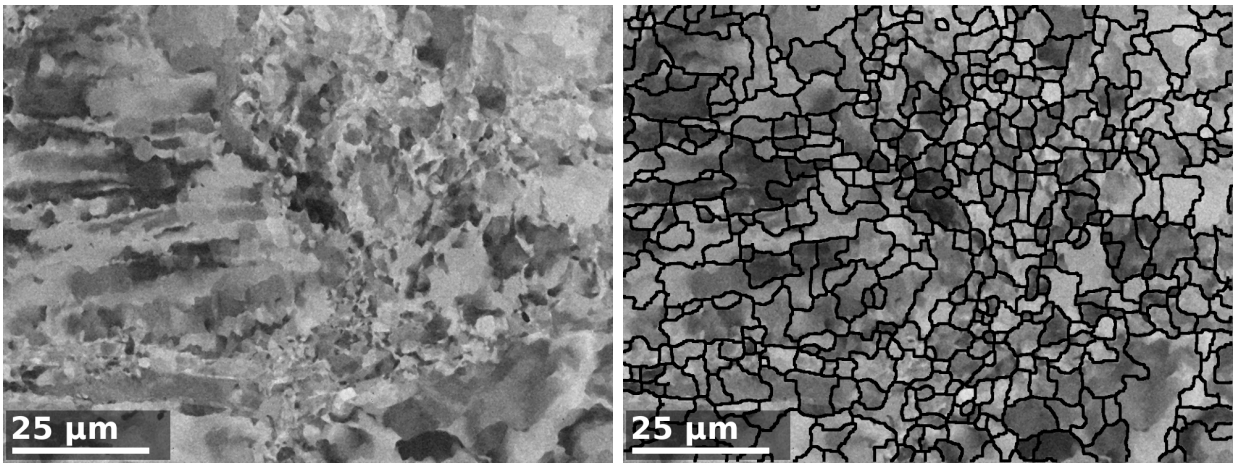

(a) (b)

Figure 18: BSE-SEM micrograph obtained on a 316L sample after hot deformation ($\varepsilon \approx 0.65$) at 1000°C and a strain rate of 0.01 s^{-1}. (a) Raw image and (b) GB network processed by image analysis superposed with the original micrograph.